

# Cross-Resolution SAR Target Detection Using Structural Hierarchy Adaptation and Reliable Adjacency Alignment

Jiang Qin, *Student Member, IEEE*, Bin Zou, *Senior Member, IEEE*,  
Haolin Li, *Student Member, IEEE*, Lamei Zhang, *Senior Member, IEEE*,

**Abstract**—In recent years, continuous improvements in SAR resolution have significantly benefited applications such as urban monitoring and target detection. However, the improvement in resolution leads to increased discrepancies in scattering characteristics, posing challenges to the generalization ability of target detection models. While domain adaptation technology is a potential solution, the inevitable discrepancies caused by resolution differences often lead to blind feature adaptation and unreliable semantic propagation, ultimately degrading the domain adaptation performance. To address these challenges, this paper proposes a novel SAR target detection method (termed *CR-Net*), that incorporates structure priors and evidential learning theory into the detection model, enabling reliable domain adaptation for cross-resolution detection. To be specific, *CR-Net* integrates Structure-induced Hierarchical Feature Adaptation (*SHFA*) and Reliable Structural Adjacency Alignment (*RSAA*). *SHFA* module is introduced to establish structural correlations between targets and achieve structure-aware feature adaptation, thereby enhancing the interpretability of the feature adaptation process. Afterwards, the *RSAA* module is proposed to enhance reliable semantic alignment, by leveraging the secure adjacency set to transfer valuable discriminative knowledge from the source domain to the target domain. This further improves the discriminability of the detection model in the target domain. Based on experimental results from different-resolution datasets, the proposed *CR-Net* significantly enhances cross-resolution adaptation by preserving intra-domain structures and improving discriminability. It achieves state-of-the-art (SOTA) performance in cross-resolution SAR target detection.

**Index Terms**—Cross-resolution detection, evidential learning, SAR target detection, scattering structure, unsupervised domain adaptation, uncertainty quantification.

## I. INTRODUCTION

**S**YNTHETIC Aperture Radar (SAR) achieves high-resolution imaging by actively transmitting and receiving electromagnetic waves. This unique capability allows SAR to operate effectively under adverse weather conditions and regardless of daylight, enabling all-weather and all-day imaging. These attributes have made SAR widely applicable in the field of Earth observation [1]. As one of the primary means of Earth observation, SAR target detection has been a hot topic in both research and applications. In recent years, advancements in SAR sensor technology have significantly

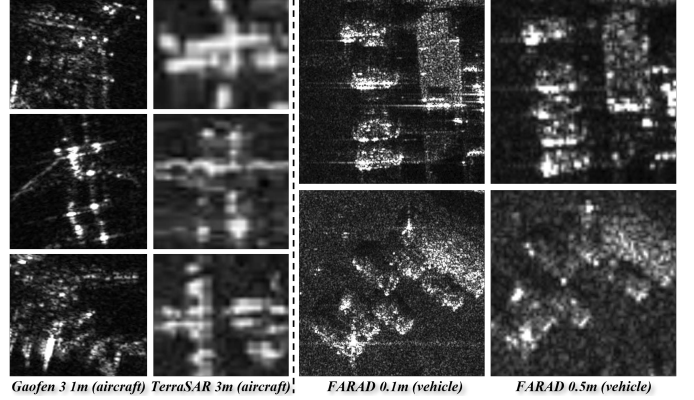


Fig. 1. Illustrating the significant scattering and scale differences in different-resolution SAR images. Targets in high-resolution images typically display finer scattering characteristics and more complex structural details, with clearer textures, and multiple scattering points. In contrast, targets in low-resolution images experience a substantial loss of detailed information and are often represented by blurred contours or key scattering points.

improved the spatial resolution of SAR images, transitioning from traditional meter-level resolution to sub-meter resolution. This leap forward has unlocked significant potential for more refined Earth observation applications: sub-meter resolution SAR images can capture more target details, offering substantial advantages in fine-grained tasks such as urban monitoring, disaster assessment, and target recognition.

However, the improvement in resolution also introduces new challenges, particularly regarding the model generalization problem in cross-resolution target detection tasks. As illustrated in Fig. 1, differences in resolution cause the same SAR target to exhibit significant variations in scattering characteristics and scales. For instance, targets in high-resolution images typically display finer scattering characteristics and more complex structural details, with clearer relationships among edges, textures, and multiple scattering points. In contrast, targets in low-resolution images suffer from substantial detail loss and are generally characterized by blurred contours or prominent scattering centers. Restricted by these substantial discrepancies, target detection models trained on a single resolution struggle to extract discriminative features from other resolution SAR images. Specifically, when trained on low-resolution data, models tend to rely on the relatively limited structural information, resulting in the extracted features that often fail to accurately describe the complex details present in high-resolution SAR targets. Similarly, models trained on high-resolution SAR data also perform poorly on low-resolution

This work is partly supported by the National Natural Science Foundation of China under Grant 62271172. (Corresponding author: Bin Zou)

All authors are with the Department of Information Engineering, Harbin Institute of Technology, Harbin 150001, China (e-mail: qinjiang19b@163.com; zoubin@hit.edu.cn; lhl\_hit@163.com; lmzhang@hit.edu.cn)

SAR images, as their reliance on the abundant features in high-resolution SAR images leaves them lacking sufficient discriminative ability when handling low-resolution SAR targets. This bidirectional decline in generalization performance poses significant challenges for cross-resolution SAR target detection.

These challenges become particularly evident during the resolution upgrades of SAR systems. As SAR sensors advance from low to high resolution, existing detection models often struggle to adapt to the newly acquired high-resolution data, making it difficult to enable a smooth transition in system deployment and applications. An alternative approach involves manually annotating datasets to train detection models for different resolutions. However, this process, along with creating separate annotation for varying resolution datasets, is highly resource-intensive and significantly limits the feasibility of joint analysis SAR data with different resolutions. Consequently, achieving effective generalization in cross-resolution target detection models and addressing the domain discrepancies introduced by resolution differences have become critical challenges in the field of SAR target detection.

Domain adaptation is an effective approach to address the aforementioned domain discrepancies and improve the generalization performance on the unseen data [2], [3]. The goal of this technique is to transfer the knowledge learned from the labeled source domain to an unlabeled target domain with distribution differences, ensuring satisfactory performance on the target domain data. In recent years, some advanced researches have leveraged domain adaptation techniques in SAR target detection, focusing on improving cross-modality (e.g. optical-to-SAR [4]–[6] and SAR-to-SAR [7]–[9]) detection performance. For instance, Zhao et al. [10], [11] achieved optical-to-SAR target detection by employing adversarial learning and feature decomposition to obtain domain-invariant features. Pan et al. [4] introduced an unbalanced adversarial alignment approach to address the issue of misaligned domain features, enabling ship detection from optical to SAR images. However, some researches [12], [13] have shown that adversarial learning-based domain adaptation methods negatively impact feature discriminability. To address this, some studies [8], [9], [13] have incorporated pseudo-label learning, which aligns feature distributions while enhancing feature discriminability. Additionally, other studies [7], [14], [15] have leveraged the physical priors of SAR targets to enhance SAR target detection under the guidance of prior knowledge. Wang et al. [15] utilized sub-aperture decomposition [16] and data augmentation to achieve the knowledge transfer from synthetic data to real-world data. Some researchers [7] have introduced key scattering points of targets to enable center-aware feature adaptation, improving SAR target detection across different SAR sensors. Zhang et al. [14] incorporated Fourier transform features to establish local structural relationships to enable target detection from optical to SAR images.

Although the aforementioned methods have made some progress in cross-domain SAR target detection, applying these black-box style models to cross-resolution SAR target detection still faces some critical challenges:

1) *Structural Distortions by the Blind Adaptation*: The intra-

domain SAR targets often exhibit significant structural diversity (illustrated in Fig 5) due to variations in imaging angles, target categories, and scattering characteristics. Existing domain adaptation methods typically aim to minimize domain gaps by unconditionally aligning the feature distributions between source and target domains. However, this structure-agnostic and blind distribution alignment lack interpretability and overlook dataset-specific structural variations, potentially distorting critical distribution structures. These structural distortions degrade the discriminability of target domain features for detection tasks. To address this, it is essential to introduce structure-aware methods that can quantify and leverage these structural differences, guiding the domain adaptation process to alleviate distribution distortions and preserve the discriminability.

2) *Risky Semantic Propagation by the Unreliable Predictions*: In unsupervised domain adaptation, the model relies heavily on the source domain for discriminating targets, often resulting in unreliable predictions for the unlabeled target domain. These unreliable predictions may serve as erroneous reference points during the adaptation process, propagating the semantic information to incorrect target instances. Such risky semantic propagation further amplifies prediction unreliability and degrades the discriminability, ultimately leading to sub-optimal performance in the target domain. Consequently, improving the reliability of the adaptation process and promoting reliable semantic discriminability are essential for mitigating error propagation and achieving robust domain adaptation.

To address the aforementioned challenges, this paper proposes *CR-Net* for cross-resolution SAR target detection that incorporates evidential learning theory and structural constraints. This approach effectively mitigates the issues of structural distortion and risky semantic propagation caused by traditional blind feature adaptation. The main contributions of this paper are as follows:

- 1) We incorporate evidence learning theory into the SAR target detection model by leveraging the Dirichlet distribution to estimate uncertainty. This enables the model to perceive uncertainty in its predictions, laying a solid foundation for subsequent reliable domain adaptation.
- 2) A scattering structure distance is proposed to quantify the structure similarity between SAR targets. Leveraging the scattering structure similarity of instances, a Structure-induced Hierarchical Feature Adaptation (*SHFA*) module is developed. By introducing structural constraints, *SHFA* module facilitates hierarchical feature adaptation between the source and target instances, enhancing the feature transferability and avoiding structural distortions throughout the adaptation process.
- 3) A Reliable Structural Adjacency Alignment (*RSAA*) module is proposed to capture reliable adjacency relationships by aligning semantic information between reliable neighbors across domains. *RSAA* module effectively transfers discriminative capabilities from the source domain to

the target domain, significantly improving the model's performance on the target domain while mitigating error accumulation.

- 4) The proposed method combines *SHFA* and *RSAA* modules, achieving significant performance improvements in cross-resolution SAR target detection tasks. Experimental results demonstrate that *SHFA* not only preserves the intra-domain structures but also significantly enhances the reliability and accuracy of cross-resolution detection.

The remainder of this article is organized as follows. Section II reviews related works. Section III explains how evidence learning is incorporated into SAR detection models. Building on the evidence-enhanced SAR detection framework, Section IV details the proposed adaptation method. Section V presents the experimental results and analysis. Finally, Section VI concludes the paper.

## II. RELATED WORKS

### A. Uncertainty Estimation and Evidential Learning

Uncertainty is a key factor for evaluating the predictive reliability of deep models [17]–[19]. Bayesian deep learning [20] and subsequent approximate methods [21], [22] provide theoretical and practical approaches for uncertainty modeling [20]. However, they still face challenges related to high computational cost and low efficiency. Recently, evidence learning [17], [23] has gained significant attention due to its capability to explicitly model and inference with evidence, making it a powerful approach for quantifying uncertainty. Compared to traditional Bayesian methods, evidence learning learns a Dirichlet distribution to simultaneously output predictive confidence and uncertainty, avoiding high computational costs and improving flexibility [19]. Currently, evidential learning has been widely applied to high-reliability tasks such as medical diagnosis [24] and anomaly detection [25]. However, its application in cross-resolution SAR target detection remains largely unexplored. This paper applies evidence learning in cross-resolution SAR detection tasks to model uncertainty and improve adaptation reliability across resolutions.

### B. SAR Target Detection

In SAR target detection, mainstream solutions are divided into one-stage detectors (e.g., RetinaNet [26], YOLO [27], [28], SSD [29]) and two-stage detectors (e.g., Faster RCNN [30], Sparse RCNN [31]). There are many notable advancements based on these paradigms in SAR community. Zhou et al. [32] proposed a Sidelobe-aware detection network to enhance small ship feature representation. Ju et al. [33] introduced a Polar Encoding and Decoding strategy to improve dense regression for rotated target detection, while Zhao et al. [34] improved the rotated target detection by enhancing inter-class separability [35]. Yang et al. [36] proposed a unified dynamic SAR detection framework to boost dense prediction performance in complex scenarios. For two-stage detectors, Cui et al. [37] improved multi-scale ship detection accuracy using attention mechanisms, and [38] addressed nearshore ship detection problem using an anisotropic pyramid-based saliency

enhancement algorithm. Some studies [16], [39], [40] have improved target detectors from the perspective of environmental clutters. For example, certain efforts [39] suppressed the sea clutter using frequency domain information, while Dai et al. [40] addressed low-frequency bias and enhanced high-frequency features through multi-scale dynamic learning. Additionally, some researchers [16], [41] applied data transformations or sub-aperture decomposition [16] to optimize input data quality, thereby improving target detection performance.

### C. Unsupervised Domain Adaptation

Unsupervised Domain Adaptation (UDA) is an important research direction in transfer learning, aiming to improve the performance of models on the target domain by leveraging labeled data from the source domain and unlabeled data from the target domain [2]. The core challenge lies in the distribution discrepancy (i.e., domain shift) between the source and target domains. Researchers have proposed various methods to reduce this discrepancy, including distribution alignment (e.g., DAN [2], DANN [3], MADA [42]), pseudo-label generation [13], [43], image translation methods [12], [44], [45], and mean-teacher training methods [46], [47]. UDA is widely applied in fields such as computer vision [3], [46], [48], [49], natural language processing [50], medical image analysis [51], [52], remote sensing data processing [5], [9], and autonomous driving [47]. Despite significant progress, UDA still faces challenges such as interpretability [53], domain structure distortion [2], and unreliable knowledge transfer [19].

### D. UDA for SAR Target Detection

In recent years, UDA has become a popular research topic in SAR target detection. Mainstream methods include image translation [12], [54], adversarial adaptation [55], [56], and pseudo-label learning [8], [9]. For image translation based UDA [54], some researchers [8], [55] adopted CycleGAN [57] to generate translation images to reduce domain discrepancies. Zhang et al. [5] utilized Fourier transform to create pseudo-SAR images for alignment, while others [6] added speckle noise to optical images to mitigate domain discrepancies. Adversarial adaptation aligns domain features via adversarial learning [3]. Some efforts integrate adversarial adaptation with feature decoupling [11] or context relationships [10] to improve knowledge transfer. Liu et al. [56] leverage semantic calibration and adversarial feature alignment to enhance cross-domain ship detection. To address feature discriminability issues of adversarial learning, some efforts [8], [9] introduced pseudo-label learning strategies to mitigate feature degradation, while Dong et al. [58] leveraged attention mechanisms to improve transfer performance. Despite these advancements, UDA still has limitations. On one hand, unconditioned blind adaptation of UDA may lead to distortion of domain structures. On the other hand, The discriminative capability of most UDA methods are overly biased to the source domain. Directly applying such biased knowledge to the target domain can result in unreliable predictions, and aligning these unreliable predictions may even cause risky semantic propagation.

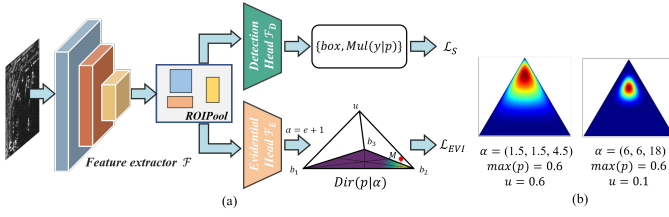


Fig. 2. The architecture of the detection model enhanced by evidential learning. (a) illustrate the model design. (b) shows the probability simplex with the same probability  $\max(p) = 0.6$  but different uncertainties. The probability  $\max(p)$  alone does not fully reflect the model's confidence, while the uncertainty  $u$  provides a more comprehensive assessment of the prediction reliability.

### III. DETECTION MODEL ENHANCED BY EVIDENTIAL LEARNING

To facilitate reliable cross-domain knowledge transfer, we first integrate the evidential learning into the target detection model, as illustrated in Fig. 2. This model mainly consists of three parts: the feature extractor  $\mathcal{F}$ , the detection branch  $\mathcal{F}_D$  and the evidential learning branch  $\mathcal{F}_E$ .

#### A. Evidential Modeling for Detection Model

The detection branch  $\mathcal{F}_D$  is responsible for class prediction  $y$  and  $\text{box}$  regression. Since the target class prediction satisfies the characteristics of a Multinomial distribution, the class probability  $p$  can be modeled as parameters of the Multinomial distribution [17], [19], which is expressed as:  $y \sim P(y | p) = \text{Mul}(y | p)$ .

The evidential learning branch  $\mathcal{F}_E$ , as shown in Fig. 2, is primarily designed to enhance the model's reliability and quantify uncertainty. By introducing the Dirichlet distribution, it models the class probability to capture the confidence in the model's predictions. The Dirichlet distribution  $\text{Dir}(p | \alpha)$ , as a conjugate prior of the Multinomial distribution, is defined as:

$$p \sim P(p | \alpha) = \text{Dir}(p | \alpha) = \begin{cases} \frac{1}{\beta(\alpha)} \prod_{c=1}^C p_c^{\alpha_c - 1}, & \text{if } p \in S_C, \\ 0, & \text{otherwise.} \end{cases} \quad (1)$$

$\beta(\alpha)$  is the Beta function for the  $C$ -dimensional Dirichlet distribution.  $\alpha = [\alpha_1, \dots, \alpha_C]$  represents the concentration parameters of the Dirichlet distribution.  $S_C$  is  $\{C - 1\}$ -dimensional unit simplex. In evidential learning, the concentration parameter  $\alpha = e + 1$ , where the evidence score  $e$  is predicted by the evidential learning branch  $\mathcal{F}_E$ .  $e \geq 0$ , representing the evidence for class predictions. The belief mass  $b_c$  and uncertainty  $u$  for a sample  $x$  are defined as:

$$b_c = \frac{e_c}{S}, u = \frac{C}{S}, \quad (2)$$

where  $S = \sum_{c=1}^C e_c + C$ , representing the Dirichlet strength. When the belief mass  $b_c$  is larger, it indicates that more evidence  $e_c$  is assigned to class  $c$ . The discriminative probability of  $c$ -th class is  $p_c = \alpha_c / S$ . A larger Dirichlet strength  $S$  reduces the overall uncertainty  $u$ , increasing the confidence and reliability in class predictions.

#### B. Model Optimization Using Source Data

Based on the Multinomial distribution  $P(y | p) = \text{Mul}(y | p)$  and the Dirichlet distribution  $P(p | \alpha) = \text{Dir}(p | \alpha)$ , the process of predicting class label  $y$  via Bayesian inference can be expressed as:

$$P(y | \alpha) = \frac{P(y, p | \alpha)}{P(p | \alpha, y)}. \quad (3)$$

According to Jensen's inequality and derivations, we have:

$$\begin{aligned} \log P(y | \alpha) &\geq \mathbb{E}_{p \sim Q(p | \alpha)} \log P(y | \alpha) \\ &= \text{KL}(Q(p | \alpha) \| P(p | \alpha, y)) \\ &\quad + \mathbb{E}_{p \sim Q(p | \alpha)} \log P(y | p) \\ &\quad + \mathbb{E}_{p \sim Q(p | \alpha)} \log \frac{P(p | \alpha)}{Q(p | \alpha)}. \end{aligned} \quad (4)$$

Here,  $p \sim Q(p | \alpha)$  is predicted by the evidential learning branch  $\mathcal{F}_E$ . Due to the non-negativity of the KL divergence, the likelihood  $\mathbb{E}_{p \sim Q(p | \alpha)} \log P(y | \alpha)$  can be maximized by optimizing the second and third terms of Eq. 4.

The second term of Eq. 4 is the integral of the cross-entropy function over  $Q(p | \alpha)$ . By substituting the Dirichlet distribution  $\text{Dir}(p | \alpha)$  for  $Q(p | \alpha)$ , this term can be derived as

$$\mathbb{E}_{p \sim Q(p | \alpha)} \log P(y | p) = - \sum_{c \in C} y_c ((\psi(S) - \psi(\alpha_c))). \quad (5)$$

Here, digamma function  $\psi(x) \approx \ln x - \frac{1}{2x}$ .

The third term of Eq. 4 represents an important prior regularization, which is equivalent to  $\text{KL}(Q(p | \alpha) \| P(p | \alpha))$ . Here,  $P(p | \alpha)$  is the Dirichlet distribution, and its concentration parameter satisfies  $\alpha \geq 1$ . For class prediction problems, an ideal Dirichlet distribution  $P(p | \alpha)$  should concentrate on the vertex of the simplex corresponding to the true class  $y$ . In other words, apart from class  $y$ , the concentration parameter  $\alpha$  for other classes should be minimized to 1. Therefore, the prior regularization is formulated as:

$$\text{KL}(Q(p | \alpha) \| P(p | \alpha)) \approx \text{KL}(\text{Dir}(p | \hat{\alpha}) \| \text{Dir}(p | [1, \dots, 1])). \quad (6)$$

Here  $\hat{\alpha} = y_c + (1 - y_c) \alpha_c$ , where  $\hat{\alpha}$  for the true label  $y_c$  is set to 1, while  $\hat{\alpha}$  for the remaining classes are maintained as predicted by the model. The goal is to minimize Eq. 6 to reduce evidence for incorrect classes.

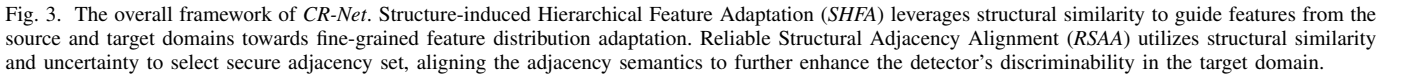
Given the source domain data  $\mathcal{X}_S$ , the overall optimization objective for the evidential learning branch is expressed as:

$$\begin{aligned} \mathcal{L}_{EVI} &= \frac{1}{|\mathcal{X}_S|} \sum_{x \in \mathcal{X}_S} \sum_{c=1}^C y_c (\psi(S) - \psi(\alpha_c)) \\ &\quad + \text{KL}(\text{Dir}(p | \alpha) \| \text{Dir}(p | [1, \dots, 1])). \end{aligned} \quad (7)$$

For parameter optimization of the target task detection branch  $\mathcal{F}_D$ , the target detection loss  $\mathcal{L}_S$  can be directly used to optimize the model. For the evidential learning branch  $\mathcal{F}_E$ , its parameters can be optimized by minimizing  $\mathcal{L}_{EVI}$ . Therefore, the total supervised loss for the source domain is presented as:

$$\mathcal{L} = \mathcal{L}_S + \mathcal{L}_{EVI}. \quad (8)$$




$$d_{ST} = \frac{\sum_{n=1}^N \sum_{m=1}^M f_{n,m} \cdot \sqrt{(x_n - x_m)^2 + (y_n - y_m)^2}}{\sum_{n=1}^N \sum_{m=1}^M f_{n,m}}.$$

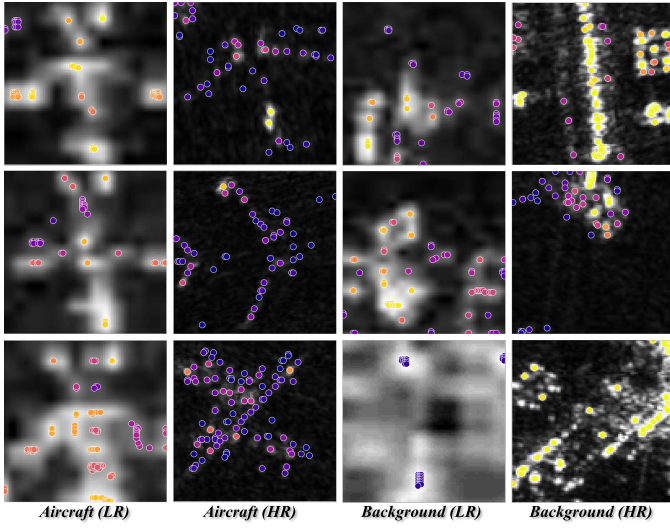


Fig. 4. Scattering structures of foreground and background in low-resolution (LR) and high-resolution (HR) images. All images are resized to the same size for better comparison. Color indicates scattering intensity, ranging from blue (low) to yellow (high). Although the scattering features of LR and HR targets differ, the structural similarity remains (e.g. aircraft targets exhibit a cross-shaped pattern).

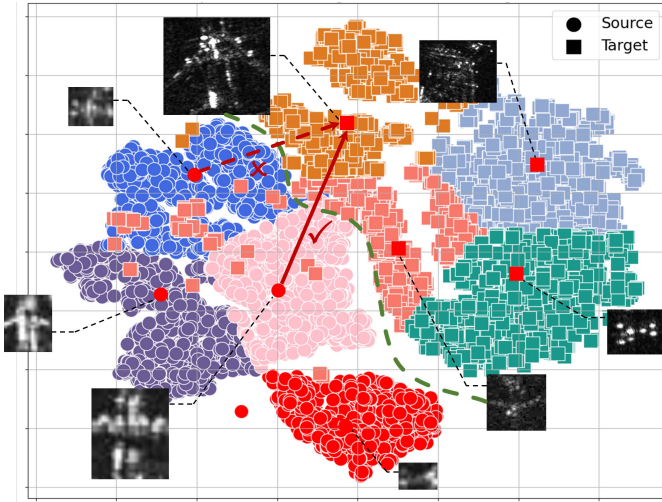


Fig. 5. Feature distributions visualized by t-SNE [61] in the source and target domains. Clusters in different colors represent targets belonging to the same category but exhibiting different patterns due to structure variations. Directly aligning the overall feature distributions while disregarding intra-domain structural differences may result in misalignment between patterns with distinct structures, leading to negative transfer and hindering the achievement of optimal performance.

### B. Structure-induced Hierarchical Feature Adaptation

In the problem of cross-resolution domain adaptation, the data distributions between the low-resolution and high-resolution domains often exhibit multi-mode structures, as shown in the Fig 5. Due to differences in imaging azimuth angles, target categories, and scales, SAR targets of the same category exhibit significant intra-class diversity. This phenomenon is further amplified across different resolutions, making it challenging to achieve satisfactory results using traditional domain adaptation methods that directly align overall distributions. If the intra-class diversity is ignored, errors may arise due to mismatched modes between different structures,

leading to negative adaptation.

To address this issue, *SHFA* is proposed to achieve structure-aware and fine-grained feature adaptation. In principle, the feature distributions of targets with similar structures should be more closely aligned. Thus, *SHFA* utilizes physical structure similarity to explicitly guide the feature adaptation process, ensuring that features with similar structural patterns are aligned in the feature space.

Specifically, based on the scattering structure distance  $d_{ST}$  introduced earlier, we use clustering methods to obtain  $n_a$  structure anchors  $\{A_j\}_{j=1}^{n_a}$ , representing typical structures observed in the source domain data. Examples of these typical structures are shown in the Fig. 6. These typical structures reflect the main modes of the source domain feature distribution (visualized in Fig 5) and provide structural guidance for adapting domain features. Given the scattering point set  $P_i$  of the  $i$ -th instance, we can calculate the structural similarity  $sim_{i,j}$  between this instance and each structure anchor  $A_j$ , which quantifies the relationship between the  $i$ -th instance and the  $j$ -th typical structures:

$$sim_{i,j} = \max \left( \frac{e^{-d_{ST}(i,j)}}{\sum_{j=1}^{n_a} e^{-d_{ST}(i,j)}}, \delta \right). \quad (9)$$

Here,  $\delta = 0.1$  is a margin parameter, used to keep structural similarity non-negative.  $sim_{i,j} \in [\delta, 1]$ . A higher  $sim_{i,j}$  value indicates a greater structural similarity between instance  $i$  and the structure anchor  $A_j$ . Each structure anchor  $A_j \in \{A_j\}_{j=1}^{n_a}$  is associated with a domain discriminator  $\mathcal{D}_j$ , which is responsible for hierarchical feature adaptation corresponding to the structure  $A_j$ . By leveraging the structural similarity  $sim_{i,j}$ , we dynamically weight each instance feature to indicate how much the feature to be assigned to each discriminator, enabling structure-aware hierarchical feature adaptation:

$$\begin{aligned} \mathcal{L}_{INS} = & -\frac{1}{n_a} \sum_{i \in \{n_a\}} \sum_{j \in \{|\mathcal{X}^S| \cup |\mathcal{X}^T|\}} [y_j \log \mathcal{D}_i(sim_{i,j} \cdot f_j) \\ & + (1 - y_j) \log (1 - \mathcal{D}_i(sim_{i,j} \cdot f_j))], \end{aligned} \quad (10)$$

where  $y_i = 1$  indicates the target domain and  $y_i = 0$  indicates the source domain. Combined with the traditional image-level adversarial loss  $\mathcal{L}_{IMG}$  from [62], the feature adaptation loss is further expressed as:

$$\mathcal{L}_{SHFA} = \mathcal{L}_{IMG} + \mathcal{L}_{INS}. \quad (11)$$

Here, the image-level feature adaptation loss  $\mathcal{L}_{IMG}$  is defined as

$$\begin{aligned} \mathcal{L}_{IMG} = & - \sum_{j \in \{|\mathcal{X}^S| \cup |\mathcal{X}^T|\}} \sum_{u,v} [y_j \log \mathcal{D}_{IMG}(f_j(u,v)) \\ & + (1 - y_j) \log (1 - \mathcal{D}_{IMG}(f_j(u,v)))] \end{aligned} \quad (12)$$

$\mathcal{D}_{IMG}$  is the image-level domain discriminator.  $f_j(u,v)$  is the image-level feature of the spatial location  $(u,v)$ .

### C. Reliable Structural Adjacency Alignment

The *RSAA* module is proposed to further enhance the discriminative capability of the detector in the target domain.

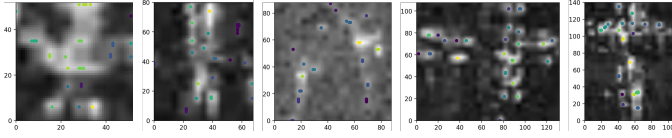


Fig. 6. Examples of typical structures observed in the TerraSAR dataset ( $n_a = 5$ ).

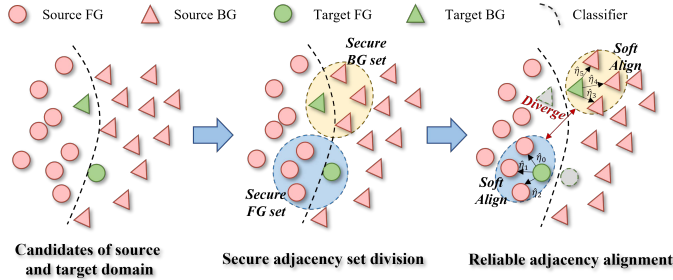


Fig. 7. Illustration of RSAA process. ‘FG’ and ‘BG’ denotes the abbreviation of foreground and background respectively. Aligning the target domain instance with its source domain neighbors enables the detector better discriminative capability in the target domain.

The core idea of the RSAA module is that reliable neighbors in the feature space share the same semantics. Therefore, as shown in Fig. 7, RSAA improves discriminability in the target domain by selecting the secure adjacency set from the source domain and aligning the semantics between target instances and the adjacency neighbors. Compared with traditional hard feature alignment methods, RSAA effectively alleviates the risky semantic propagation and error accumulation.

Given a target domain instance  $x^T \in \mathcal{X}^T$ , we define the  $r$ -adjacency set of  $x^T$  as  $R_r(x^T) = \{x^T\} \cup \{N_r(x^T)\}$ , where  $N_r(x^T)$  is the  $r$  nearest source domain neighbors of the target domain instance  $x^T$ . Specifically:

$$N_r(x^T) = \{x_j^S | j \in \text{Top-}r(f^T \otimes \{f_n^S\}_{n=1}^{n_f})\}, \quad (13)$$

where  $\otimes$  denotes cosine similarity.  $\{f_n^S\}_{n=1}^{n_f}$  is the source feature bank  $\{f_n^S, p_n^S, u_n^S, p_n^S\}_{n=1}^{n_f}$ .  $f_n^S$  and  $p_n^S$  are the source instance feature and its scattering point set, respectively, while  $u_n^S$  and  $p_n^S$  are the predicted uncertainty and probability. To measure the reliability of each instance  $x^T$  and its adjacency set  $R_r(x^T)$ , there are two factors defined: reliable instance factor  $\hat{\eta}$  and secure adjacency factor  $\hat{\gamma}$ .

1) *Reliable Instance Factor  $\hat{\eta}$* : As introduced in Section III-A, lower uncertainty  $u$  indicates the prediction is more reliable. Given the uncertainty  $u(x_i^T)$  and its predicted probability  $p_i^T$  of instance  $x_i^T$ , the reliable instance factor  $\hat{\eta}$  for a target domain instance is defined as:

$$\hat{\eta}(x_i^T) = p_i^T \cdot e^{(-u(x_i^T)/k)}. \quad (14)$$

Here,  $k$  is the scaling factor. When the uncertainty  $u$  is lower, the reliable instance factor  $\hat{\eta}$  becomes higher, indicating that the prediction for the instance  $x_i^T$  is more reliable. Such instance is more suitable to be assigned greater weights, while less reliable instances are penalized during semantic alignment. This helps to avoid error accumulation caused by unreliable predictions.

2) *Secure Adjacency Factor  $\hat{\gamma}$* : It is used to select the secure adjacency set of each target domain instance  $x^T$ , making it suitable for adjacency semantic alignment. We hypothesize that both structural and perceptual consistency are essential for a secure adjacency set. 1) *Structural consistency*: instances within the secure adjacency set exhibit structural consistency. 2) *Perceptual consistency*: instances within the secure adjacency set have similar levels of reliability. If both conditions are satisfied, we consider the adjacency set as a secure set, indicating the adjacency set has high-level structural and perceptual consistency. Based on these two hypotheses, the RSAA  $\hat{\gamma}(x_i^T)$  is defined from both structural and perceptual perspectives:

$$\hat{\gamma}(x_i^T) = \{\hat{\gamma}_{ST}(x_i^T), \hat{\gamma}_u(x_i^T)\}. \quad (15)$$

Here,

$$\hat{\gamma}_{ST}(x_i^T) = \log \left( 1 + \frac{\max_{a \neq b, a, b \in |\tilde{D}_{ST}|} \|\tilde{D}_{ST}(a) - \tilde{D}_{ST}(b)\|_1}{\min_{a \neq b} \|\tilde{D}_{ST}(a) - \tilde{D}_{ST}(a)\|_1 + \epsilon} \right),$$

$$\hat{\gamma}_u(x_i^T) = \log \left( 1 + \frac{\max_{x_i \neq x_j, x_i, x_j \in R_r(x_i^T)} \|u(x_i) - u(x_j)\|_1}{\min_{a \neq b} \|u(x_i) - u(x_j)\|_1 + \epsilon} \right). \quad (16)$$

$\tilde{D}_{ST} = \{d_{ST}(i, j) | i, j \in |R_r(x_i^T)|\}$  is the set of scattering structure distances within  $R_r(x_i^T)$ . The uncertainty  $u(x_i)$  serves as a measure of the prediction reliability for neighbors within the adjacency set.  $\|\cdot\|_1$  is Manhattan distance.  $\epsilon$  is a small constant to avoid division by zero.

3) *Secure Adjacency Set Division*: The smaller  $\hat{\gamma}_{ST}(x_i^T)$  and  $\hat{\gamma}_u(x_i^T)$  indicate higher structural and semantic consistency within the  $r$ -adjacency set  $R_r(x_i^T)$ . Accordingly, the adjacency set is divided as the secure adjacency set  $R_r^{se}$ . Conversely, large  $\hat{\gamma}_{ST}(x_i^T)$  and  $\hat{\gamma}_u(x_i^T)$  values suggest a risky adjacency set, which is discarded from semantic alignment. To avoid relying on fixed thresholds, we introduce an adaptive strategy for secure adjacency set selection:

$$R_r^{ST} = \{R_r(x_i^T) | \hat{\gamma}_{ST}(x_i^T) \leq \mu_{ST} + \lambda_{se} \cdot \sigma_{ST}\},$$

$$R_r^u = \{R_r(x_i^T) | \hat{\gamma}_u(x_i^T) \leq \mu_u + \lambda_{se} \cdot \sigma_u\}. \quad (17)$$

$\mu$  and  $\sigma$  represent the mean and standard deviation of  $\hat{\gamma}$ , respectively.  $\lambda_{se}$  is a scaling hyperparameter. Finally, the secure adjacency set  $R_r^{se}$  can be obtained as the intersection of the structural and perceptual constraints:

$$R_r^{se} = R_r^{ST} \cap R_r^u. \quad (18)$$

4) *Soft Semantic Alignment*: To enhance the discriminability of detector in the target domain, the secure adjacency set  $R_r^{se}$  is further partitioned as secure foreground adjacency set  $R_r^{fg}$  and secure background adjacency set  $R_r^{bg}$  according to



the probabilities of source adjacency instances:

$$R_r^{fg} = \left\{ R_r^{se}(x_i^T) \mid \min_{x_j^S \in N_r(x_i^T)} p_j^S \geq 0.5 \right\}, \quad (19)$$

$$R_r^{bg} = \left\{ R_r^{se}(x_i^T) \mid \min_{x_j^S \in N_r(x_i^T)} p_j^S < 0.5 \right\}.$$

Afterwards, reliable instance factor together with the secure adjacency sets  $R_r^{fg}$  and  $R_r^{bg}$  are employed for soft semantic alignment, which encourages the same semantic features to be closer and those of different semantics to be separated:

$$\mathcal{L}_{RSAA} = \frac{1}{|R_r^{se}|} \sum_{x_i^T \in R_r^{se}} \sum_{x_j^S \in N_r(x_i^T)} \hat{\eta}(x_i^T) \|f_i^T - f_j^S\|_1$$

$$+ \frac{1}{|R_r^{fg}| |R_r^{bg}|} \sum_{x_i^T \in R_r^{fg}} \sum_{x_j^T \in R_r^{bg}} \max(\varsigma - \|\bar{f}_i^{fg} - \bar{f}_j^{bg}\|_1, 0). \quad (20)$$

$\varsigma = 0.2$  is the margin parameter.  $\bar{f}_i^{fg}$  and  $\bar{f}_j^{bg}$  represent the average foreground feature and the average background feature respectively within the secure set. By minimizing  $\mathcal{L}_{RSAA}$ , the target domain instance  $x^T$  gains discriminative knowledge from source reliable neighbors in the secure set  $R_r^{se}$ , thereby enhancing the performance of the detector in the target domain.

#### D. Overall Training Objective

In summary, to achieve cross-resolution SAR target detection, the overall optimization objective of our method can be expressed as:

$$\mathcal{L}_{\text{overall}} = \mathcal{L}_S + \mathcal{L}_{EVI} + \lambda_{SHFA} \mathcal{L}_{SHFA} + \lambda_{RSAA} \mathcal{L}_{RSAA}, \quad (21)$$

where  $\lambda_{SHFA}$  and  $\lambda_{RSAA}$  are hyper-parameters that balance the contributions of each component. The training process is detailed in Alg. 2.

### V. EXPERIMENTS AND ANALYSIS

#### A. Datasets Descriptions

In this experiment, SAR images with different resolutions are used to construct cross-resolution SAR target detection tasks. The specific data configurations are shown in Table I. The experimental dataset includes Gaofen-3 aircraft data (1 m resolution) from [63], TerraSAR aircraft data (3 m resolution) from [64], and FARAD vehicle data (0.5 m and 0.1 m resolutions) from [9], [65]. During the data preprocessing stage, to establish a unified cross-resolution target detection benchmark, we first used a bilinear interpolation algorithm to up-sample the low-resolution images to match the sizes of the corresponding high-resolution images. Subsequently, the images were cropped into  $256 \times 256$  image patches. Based on the various resolution SAR data shown in Table I and adhering to the principle of consistency in target categories between the source and target domains, we constructed four cross-resolution target detection tasks to verify the effectiveness of the proposed method. The cross-resolution detection task configurations are detailed in Table II.

#### Algorithm 2 Training process of CR-Net.

- Input:** Labeled source domain data  $\{x^S, y^S\}$  and unlabeled target domain data  $x^T$ , feature extractor  $\mathcal{F}$ , detection branch  $\mathcal{F}_D$ , evidential branch  $\mathcal{F}_E$ , domain discriminator  $\mathcal{D}$ , training epochs  $N_{\text{epoch}}$ .
- Output:** Well-trained  $\mathcal{F}$ ,  $\mathcal{F}_D$ .
1. Initialize parameters of  $\mathcal{F}$ ,  $\mathcal{F}_D$ ,  $\mathcal{F}_E$ , and  $\mathcal{D}$ .
  2. Construct scattering structure anchors  $\{A_j^n\}_{j=1}^a$  from  $\{x^S, y^S\}$ .
  3. **for**  $n = 1$  to  $N_{\text{epoch}}$  **do**
  4.   Calculate  $\mathcal{L}_{EVI}$  and  $\mathcal{L}_S$  by Eq. 8 using  $x^S$  and  $y^S$ ;
  5.   Take gradient descent  $\nabla_{\{\mathcal{F}, \mathcal{F}_E\}} \mathcal{L}_{EVI} + \nabla_{\{\mathcal{F}, \mathcal{F}_D\}} \mathcal{L}_S$ ;
  6.   Update  $\mathcal{F}$ ,  $\mathcal{F}_E$  and  $\mathcal{F}_D$ ;
  7.   Calculate structure similarity by Alg. 1 and Eq. 9;
  8.   Calculate  $\mathcal{L}_{SHFA}$  by Eq. 11;
  9.   Take gradient descent  $\nabla_{\{\mathcal{D}\}} \mathcal{L}_{SHFA} - \nabla_{\{\mathcal{F}\}} \mathcal{L}_{SHFA}$ ;
  10.   Update  $\mathcal{F}$  and  $\mathcal{D}$ ;
  11.   **if**  $n > N_{\text{epoch}}/2$  **then**
  12.     Generate  $r$ -adjacency of  $x^T$ ;
  13.     Compute  $\mathcal{L}_{RSAA}$  using Eq. 20;
  14.     Take gradient descent  $\nabla_{\{\mathcal{F}, \mathcal{F}_D\}} \mathcal{L}_{RSAA}$ ;
  15.     Update  $\mathcal{F}$  and  $\mathcal{F}_D$ ;
  16.   **end if**
  17. **end for**
  18. **return**  $\mathcal{F}$  and  $\mathcal{F}_D$ .

TABLE I  
TECHNICAL PARAMETERS OF DIFFERENT RESOLUTION SAR SENSORS.

Sensor	Gaofen-3	TerraSAR	FARAD (HR)	FARAD (LR)
Imaging platform	Spaceborne	Spaceborne	Airborne	Airborne
Band	C	X	Ka	Ka
Resolution	1m $\times$ 1m	3m $\times$ 3m	0.1m $\times$ 0.1m	0.5m $\times$ 0.5m
Target type	Aircraft	Aircraft	Vehicle	Vehicle
Slice number	3500	2674	1265	1129

#### B. Implementation Details

All experiments were conducted on a server equipped with an NVIDIA A6000 GPU with 48GB of memory. During the training phase, labeled source domain data and unlabeled target domain data were jointly input into the target detection model for training, and all methods were trained for 10 epochs. The initial learning rate was set as 0.002, and decreased to 0.001 after 5 epochs. In the testing phase, the target domain data were used to evaluate the detection performance. The evaluation metrics we adopted include VOC mAP, F1 score, Precision, and Recall. In all experiments, the IoU threshold for calculating mAP was set to 0.5. Hyper-parameter  $\lambda_{SHFA} = 0.5$ ,  $\lambda_{RSAA} = 0.5$ ,  $\lambda_{se} = -1$ ,  $k = 30$ ,  $n_a = 5$ ,  $r = 5$  for Aircraft tasks, and  $r = 3$  for Vehicle tasks. Details are discussed in Section V-F.

#### C. Comparisons and Analysis

To ensure the fairness of the experiments, all comparison methods were implemented using the Faster RCNN detector, and comparative experiments were conducted based on the four cross-resolution target detection tasks shown in Table II.

TABLE II  
CROSS-RESOLUTION DETECTION TASKS IN THE EXPERIMENTS. ‘LR’  
DENOTES LOW RESOLUTION. ‘HR’ DENOTES HIGH RESOLUTION.

Task	Source Domain Data	Target Domain Data
Aircraft LR→HR	TerraSAR (3m × 3m)	Gaofen-3 (1m × 1m)
Aircraft HR→LR	Gaofen-3 (1m × 1m)	TerraSAR (3m × 3m)
Vehicle LR→HR	FARAD (0.5m × 0.5m)	FARAD (0.1m × 0.1m)
Vehicle HR→LR	FARAD (0.1m × 0.1m)	FARAD (0.5m × 0.5m)

1) *Quantitative comparisons*: From the quantitative results in Table III and Table IV, it is clear that the performance of Faster RCNN without domain adaptation is significantly lower than that of other methods. This demonstrates that discrepancies across resolutions can lead to a marked decline in SAR target detection performance. Moreover, five cross-domain detection methods perform significantly better than the baseline Faster RCNN, validating the feasibility and effectiveness of domain adaptation-based approaches in cross-domain target detection tasks.

According to Table III, HSANet and DAF perform poorly in the Aircraft LR→HR and Aircraft HR→LR tasks. This is because these cross-resolution detection tasks involve a greater diversity in target scales, which increases the challenge of cross-resolution target detection. In contrast, the proposed *CR-Net* outperforms the other four SOTA cross-domain detection methods across all evaluation metrics. This not only highlights the effectiveness of *CR-Net* in cross-resolution detection tasks, but also further validates its robustness and performance advantages in addressing resolution distribution discrepancies. In the Aircraft LR→HR task, *CR-Net* achieves over a 25% improvement in Recall, Precision, and F1 score compared to the second-best method, GPANet. For the Aircraft LR→HR task, our method achieves over a 28% improvement in Precision, while for the Aircraft HR→LR task, the improvement is approximately 13%. These results demonstrate that our method significantly enhances the detector’s discriminability. This is achieved by aligning feature distributions effectively by *SHFA* and effectively selecting high-quality discriminative instances by *RSAA*.

As for Vehicle LR→HR and Vehicle HR→LR results from Table IV, the mAP scores are similar to F1 scores. This similarity can be attributed to the relatively uniform scale distribution of vehicles in the dataset, which reduces the challenge of bounding box regression. Nevertheless, our method still achieves the best performance compared to other methods in both tasks. Specifically, in the Vehicle LR→HR task, our method achieves 0.713 F1 score, outperforming the second-best method, IDA, by approximately 12%. This substantial improvement demonstrates that our approach is not only suitable for addressing resolution discrepancies in meter-level datasets, but also effective for cross-resolution target detection in sub-meter, very high-resolution datasets.

2) *Qualitative comparisons*: The Precision-Recall (PR) curves of five methods across four different cross-domain detection tasks are shown in Fig. 8. The PR curves show that the area under the curve (AUC) of our method is significantly larger across all tasks, demonstrating its superiority. Addition-

TABLE III  
STATISTIC COMPARISONS WITH SOTA UDA METHODS ON AIRCRAFT  
TASKS. THE BOLD FIGURE DENOTES THE BEST SCORE. THE UNDERLINE  
INDICATES THE SECOND-BEST PERFORMANCE.

Task	Method	Recall	Precision	mAP	F1
Aircraft LR→HR	Faster RCNN [30]	0.171	0.280	0.145	0.211
	DAF [62]	0.250	0.453	0.252	0.322
	GPANet [66]	<u>0.494</u>	<u>0.563</u>	<u>0.490</u>	<u>0.526</u>
	IDA [4]	0.226	0.570	0.210	0.323
	HSANet [5]	0.243	0.389	0.195	0.299
	Ours method	<b>0.658</b>	<b>0.722</b>	<b>0.563</b>	<b>0.688</b>
Aircraft HR→LR	Faster RCNN [30]	0.326	0.437	0.240	0.373
	DAF [62]	0.415	0.428	0.309	0.422
	GPANet [66]	<u>0.495</u>	<u>0.601</u>	<u>0.448</u>	<u>0.543</u>
	IDA [4]	0.462	0.545	0.402	0.500
	HSANet [5]	0.363	0.578	0.336	0.446
	Ours method	<b>0.657</b>	<b>0.685</b>	<b>0.524</b>	<b>0.671</b>

TABLE IV  
STATISTIC COMPARISONS WITH SOTA UDA METHODS ON VEHICLE  
TASKS. THE BOLD FIGURE DENOTES THE BEST SCORE. THE UNDERLINE  
INDICATES THE SECOND-BEST PERFORMANCE.

Task	Method	Recall	Precision	mAP	F1
Vehicle LR→HR	Faster RCNN [30]	0.583	0.449	0.578	0.574
	DAF [62]	0.613	0.546	0.601	0.590
	GPANet [66]	0.624	0.587	0.614	0.604
	IDA [4]	<u>0.709</u>	<u>0.595</u>	<u>0.668</u>	<u>0.632</u>
	HSANet [5]	0.702	0.541	0.641	0.590
	Ours method	<b>0.723</b>	<b>0.676</b>	<b>0.718</b>	<b>0.713</b>
Vehicle HR→LR	Faster RCNN [30]	0.337	0.545	0.271	0.416
	DAF [62]	0.480	0.483	0.433	0.482
	GPANet [66]	0.524	0.487	0.432	0.505
	IDA [4]	<u>0.560</u>	<u>0.556</u>	<u>0.512</u>	<u>0.558</u>
	HSANet [5]	0.471	<u>0.607</u>	0.429	0.531
	Ours method	<b>0.706</b>	<b>0.695</b>	<b>0.652</b>	<b>0.701</b>

ally, the PR curve of the proposed method is more stable compared to other methods, indicating that the detection precision remains consistent under varying recall rates, highlighting stronger generalization capabilities. Moreover, to provide an intuitive comparison, the visualization results of detection are shown in Fig 10, Fig 12, Fig 15, and Fig 18. From these visualizations, although the other four methods can detect most targets, they also exhibit a large number of false positives and missed detections. In contrast, the proposed method significantly reduces false positives and missed detections. This improvement is particularly evident in complex scenarios, where the proposed method demonstrates stronger robustness and adaptability. From the aircraft detection results shown in Fig. 10, our method demonstrates remarkable discriminative performance even in complex contextual backgrounds, such as near jet bridges. Compared with other four methods that rely solely on adversarial feature alignment, our method enhances the discriminability by leveraging reliable source discrimination knowledge on top of structure-aware feature adaptation. This improvement enables our method to achieve superior performance in complex background scenarios.

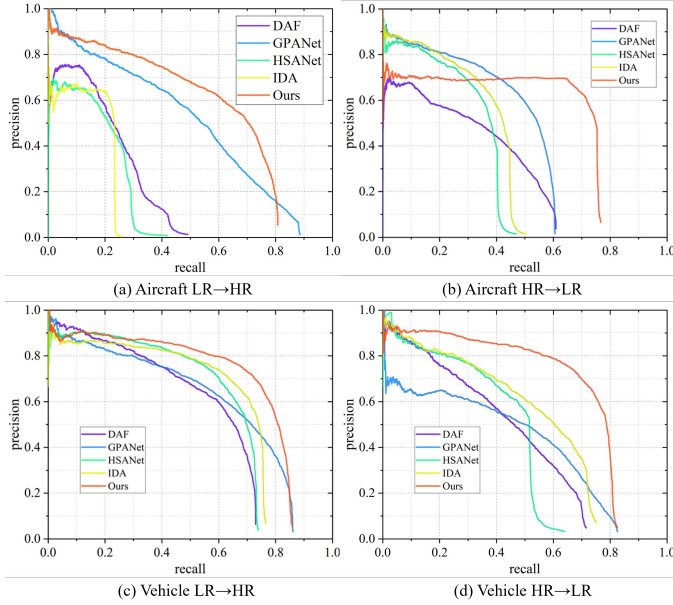


Fig. 8. Precision-Recall (PR) curves of comparison methods.

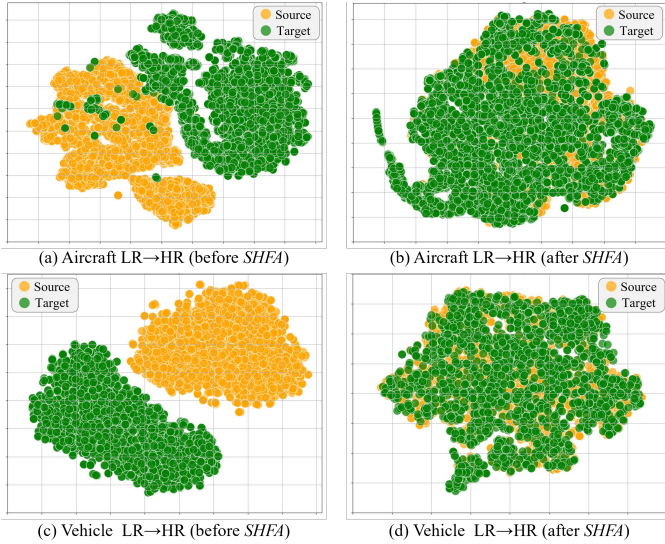


Fig. 9. Feature visualization by t-SNE [61] of instance features of source and target domain.

#### D. Ablation Studies

The ablation studies are shown in Table V. It is observed that, without introducing the *SHFA* and *RSAA* module, the baseline Faster RCNN demonstrates limited cross-resolution detection performance. This indicates that, due to resolution differences, the original target detection model fails to achieve performance generalization for cross-resolution target detection.

After introducing the *SHFA* module, the F1 score increases from 0.214 to 0.617 in the Aircraft LR→HR task). This demonstrates that the *SHFA* module effectively reduces domain discrepancies through structure-aware feature adaptation, thereby improving cross-resolution detection performance. Furthermore, with the incorporation of the *RSAA* module into the detector, the F1 score increases from 0.617 to 0.688,

TABLE V  
ABLATION STUDIES ON DIFFERENT COMPONENTS OF *CR-Net*. THE BOLD FIGURE DENOTES THE BEST SCORE.

Task	Ablations	Recall	Precision	mAP	F1
Aircraft LR→HR	Faster RCNN	0.172	0.284	0.146	0.214
	+ <i>SHFA</i>	0.589	0.648	0.530	0.617
	+ <i>RSAA</i>	0.411	0.401	0.332	0.406
	+ <i>SHFA</i> & + <i>RSAA</i>	<b>0.658</b>	<b>0.722</b>	<b>0.563</b>	<b>0.688</b>
Vehicle LR→HR	Faster RCNN	0.574	0.583	0.449	0.578
	+ <i>SHFA</i>	0.644	0.686	0.644	0.664
	+ <i>RSAA</i>	0.611	0.660	0.576	0.634
	+ <i>SHFA</i> & + <i>RSAA</i>	<b>0.723</b>	<b>0.676</b>	<b>0.718</b>	<b>0.713</b>

and the Precision rises from 0.648 to 0.722 in the Aircraft LR→HR task. The observed improvement in the Precision metric confirms that the *RSAA* module enhances the model's discriminability in the target domain, which is also verified by the results of the Vehicle LR→HR task. The integration of either *SHFA* or *RSAA* individually into the detection model leads to performance improvements, and the joint integration of both modules further achieves the most substantial benefits in cross-resolution detection performance.

#### E. Effective Analysis

1) *Effective Analysis of SHFA Module*: Fig.9 illustrates the feature adaption effects of the *SHFA* module on the Aircraft LR→HR and Vehicle LR→HR tasks. As shown in Fig.9 (a) and (c), before adaptation, the feature distributions of the source domain (orange) and the target domain (green) exhibit clear separation, with instances from the two domains forming distinct clusters. This separation reflects the presence of distribution discrepancies and intra-domain diversity, which limit the performance of cross-resolution detection. In contrast, Fig.9 (b) and (d) demonstrate that, after processing with the *SHFA* module, the feature distributions of the source and target domains show significant integration, with the distribution gap between them greatly reduced. Notably, in Fig.9 (d) for the Vehicle dataset, the source and target domain features almost completely overlap, reflecting a high degree of distribution alignment. This indicates that the *SHFA* module exhibits strong alignment capability even in tasks with complex or highly divergent distributions.

2) *Effective Analysis of RSAA Module*: According to the results shown in Fig. 11 (a), when the *RSAA* module is not used and features are directly aligned using L1 loss, the F1 score drops sharply after 1000 training iterations. When the reliable instance factor  $\hat{\eta}$  is removed (setting  $k = 0$ ), the F1 score initially increases but then decreases as training iterations progress. In contrast, when larger values ( $k = 30$  or  $k = 40$ ) are set, the F1 score steadily increases during training and shows significant improvement compared to the case without  $\hat{\eta}$ . This indicates that the reliable instance factor plays a positive role in mitigating error accumulation during the adjacency alignment process. Fig. 11 (b) illustrates the impact of the secure adjacency factor for iterative adjacency semantic alignment process. According to the definition of  $\hat{\gamma}$  in Eq. 15, the smaller  $\lambda_{se}$  indicates the stronger the filtering



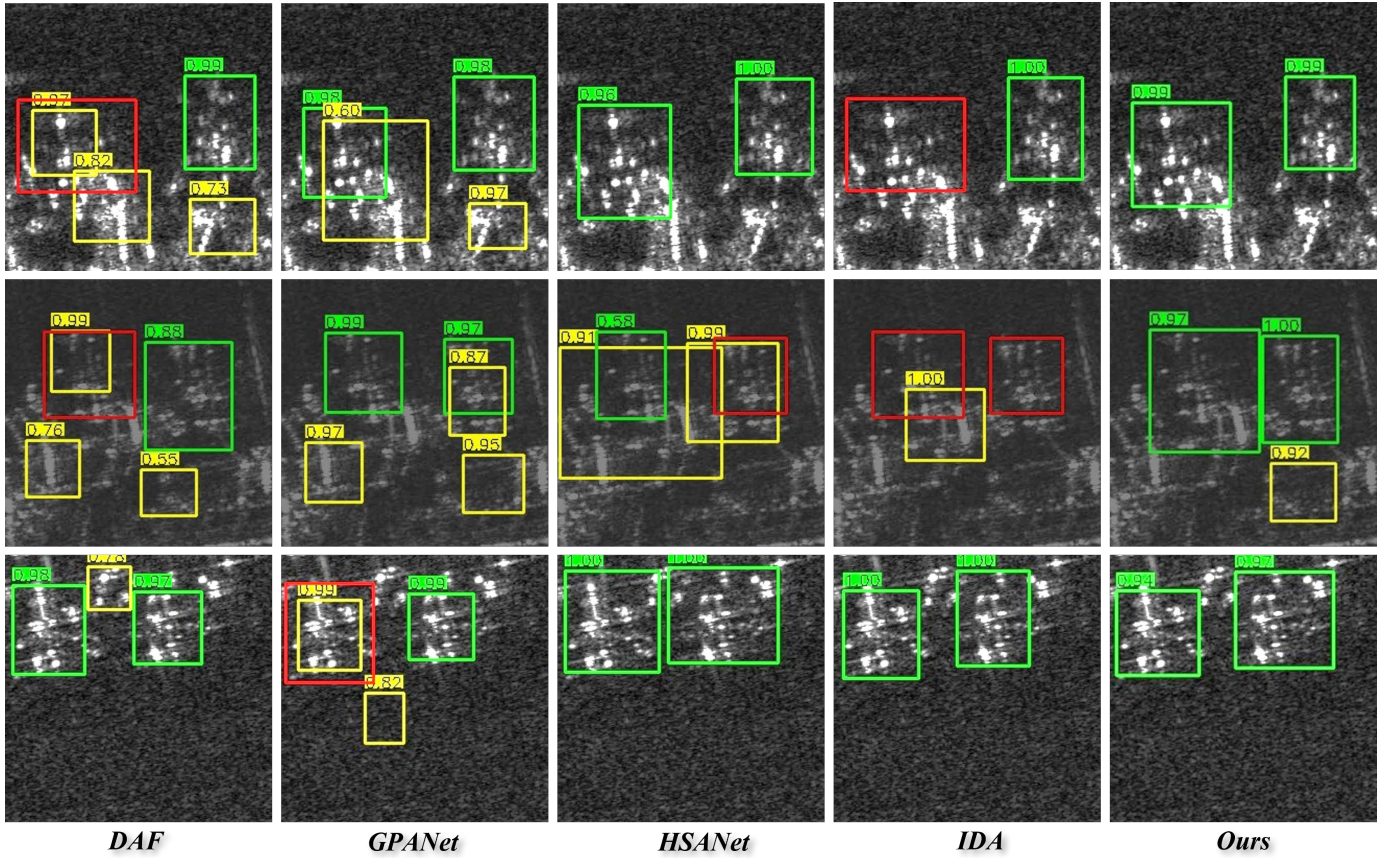


Fig. 10. Detection visualizations of different methods on the Aircraft LR→HR task. Here, in all subfigures, the green, yellow and red rectangular boxes denote correct detections, false alarms and miss detections respectively.

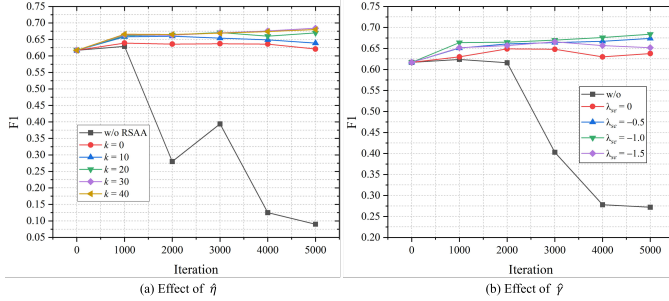


Fig. 11. The benefits of RSAA on performance during training iterations. (a) shows the effect of the reliable instance factor  $\hat{\eta}$  during the iterative process (with fixed  $\lambda_{se} = -1$ ), where ‘w/o RSAA’ in (a) represents the vanilla feature alignment using the L1 distance from Eq.20. (b) demonstrates the effect of the secure adjacency factor  $\hat{\gamma}$  on performance during the iterative process (with fixed  $k = 30$ ); ‘w/o’ in (b) indicates that the secure adjacency factor  $\hat{\gamma}$  and secure set division are not utilized for feature alignment in Eq.20.

effect on the risky set. Based on the results in Fig. 11, when  $\hat{\gamma}$  is removed, the model experiences a sharp collapse in the F1 score after approximately 2000 iterations during the adjacency semantic alignment process. In contrast, when  $\hat{\gamma}$  is introduced, the F1 score shows a gradual upward trend throughout the iterations. This demonstrates that the secure adjacency factor  $\hat{\gamma}$  helps to filter out unreliable risky sets, preventing the propagation of risky information, which is critical for reliable adjacency alignment. To acquire satisfactory performance, the

hyper-parameters are set to  $k = 30$  and  $\lambda_{Secmask} = -1$  by default, as indicated by the results in Fig. 11.

### F. Hyperparameter Discussions

1) *Discussions on Hyperparameter of SHFA:* Fig. 13 illustrates the effect of the hyperparameter  $\lambda_{SHFA}$  from Eq. 21, on cross-resolution target detection performance ( $\lambda_{RSAA} = 0$ ,  $n_a = 5$ ). The results show that both F1 score and mAP initially increase and then decrease as  $\lambda_{SHFA}$  increases, indicating that appropriate tuning of  $\lambda_{SHFA}$  is crucial for optimal model performance. For the Aircraft LR→HR and Vehicle LR→HR tasks, the best results are achieved when  $\lambda_{SHFA} = 0.5$ , where both F1 and mAP reach their highest values. When  $\lambda_{SHFA}$  is small (e.g., 0 or 0.1), the model exhibits insufficient feature adaptation capability for cross-resolution detection, resulting in lower performance. As  $\lambda_{SHFA}$  increases to 0.5, there are significant improvements in F1 and mAP, demonstrating the effectiveness of the SHFA module. However, when  $\lambda_{SHFA}$  becomes too large (e.g., 1.0 or 1.5), excessive alignment constraints may impair the model’s generalization ability to the target domain, leading to a performance drop. From the Vehicle LR→HR results in Fig. 13, the F1 and mAP of the Vehicle dataset consistently outperform those of the Aircraft dataset. This is because the Vehicle dataset exhibits a more consistent target scale distribution and more similar imaging sensor, which makes feature adaptation more feasible. According to the

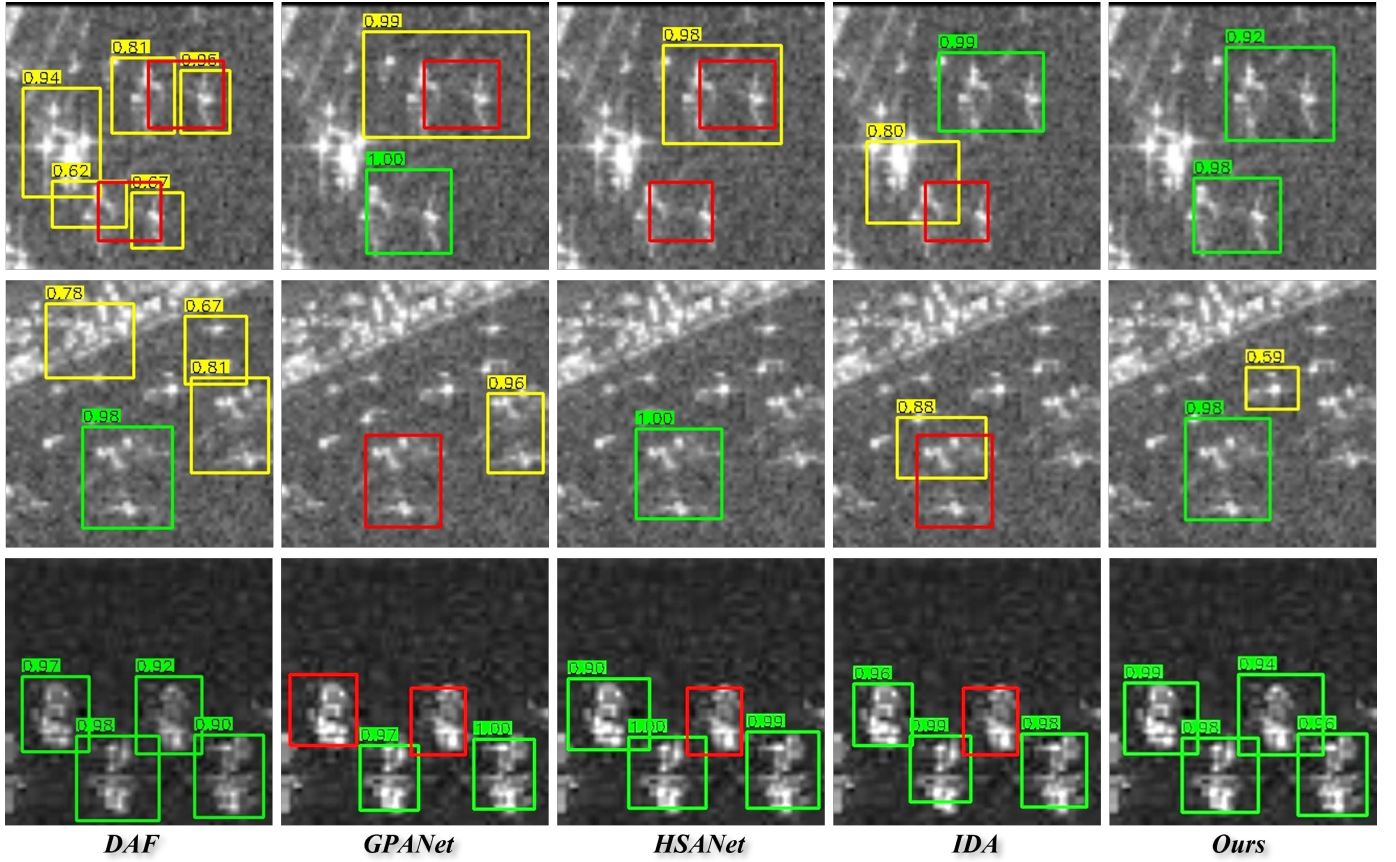


Fig. 12. Detection visualizations of different methods on the Aircraft HR→LR task. Here, in all subfigures, the green, yellow and red rectangular boxes denote correct detections, false alarms and miss detections respectively.

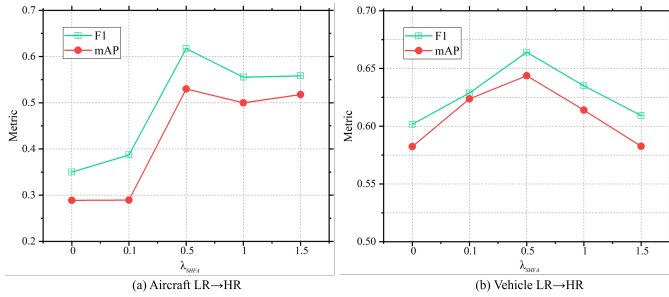


Fig. 13. Hyperparameter discussions of  $\lambda_{SHEA}$ .

aforementioned findings, it is recommended to set  $\lambda_{SHEA}$  to around 0.5 to achieve a balance between feature adaptation and generalization capability.

Fig. 14 illustrates the effect of the number of typical structures  $n_a$  (defined in Section IV-B), with  $\lambda_{SHEA} = 0.5$ . For both the Aircraft LR→HR and Vehicle LR→HR tasks, the results demonstrate that the F1 score and mAP vary with  $n_a$ . When  $n_a$  is set to 0, the *SHFA* module degenerates into a conventional single-adversarial domain adaptation model, resulting in the lowest F1 and mAP values. As  $n_a$  increases, more hierarchical discriminators are introduced into *SHFA* module, leading to improvements in both F1 and mAP. This indicates that assigning features to corresponding discriminators based on structural similarity can enhance performance.

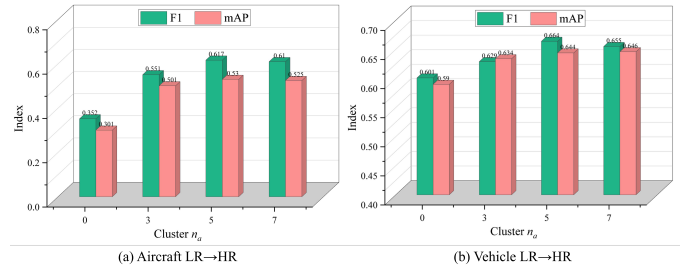


Fig. 14. Hyperparameter discussions of cluster number  $n_a$ . When  $n_a = 0$ , *SHFA* module degenerates into a conventional single-adversarial domain adaptation module.

The best results are achieved when  $n_a = 5$ , where both F1 and mAP reach their peaks. Further increasing  $n_a$  does not yield additional improvements and may even cause a slight decrease in performance. Therefore, it is recommended to set  $n_a$  to around 5 to ensure optimal performance.

2) *Discussions on Hyperparameter of RSAA*: Fig. 16 shows the impact of hyperparameter  $\lambda_{RSAA}$  (defined in Eq. 21) on cross-resolution target detection performance. In both the Aircraft LR→HR and Vehicle LR→HR tasks, as  $\lambda_{RSAA}$  increases from 0 to 0.5, F1 and mAP gradually reach their peak values. These indicate that, under an appropriate adjacency semantic alignment strength, *RSAA* can effectively enhance the detector's discriminative capability in the target domain.



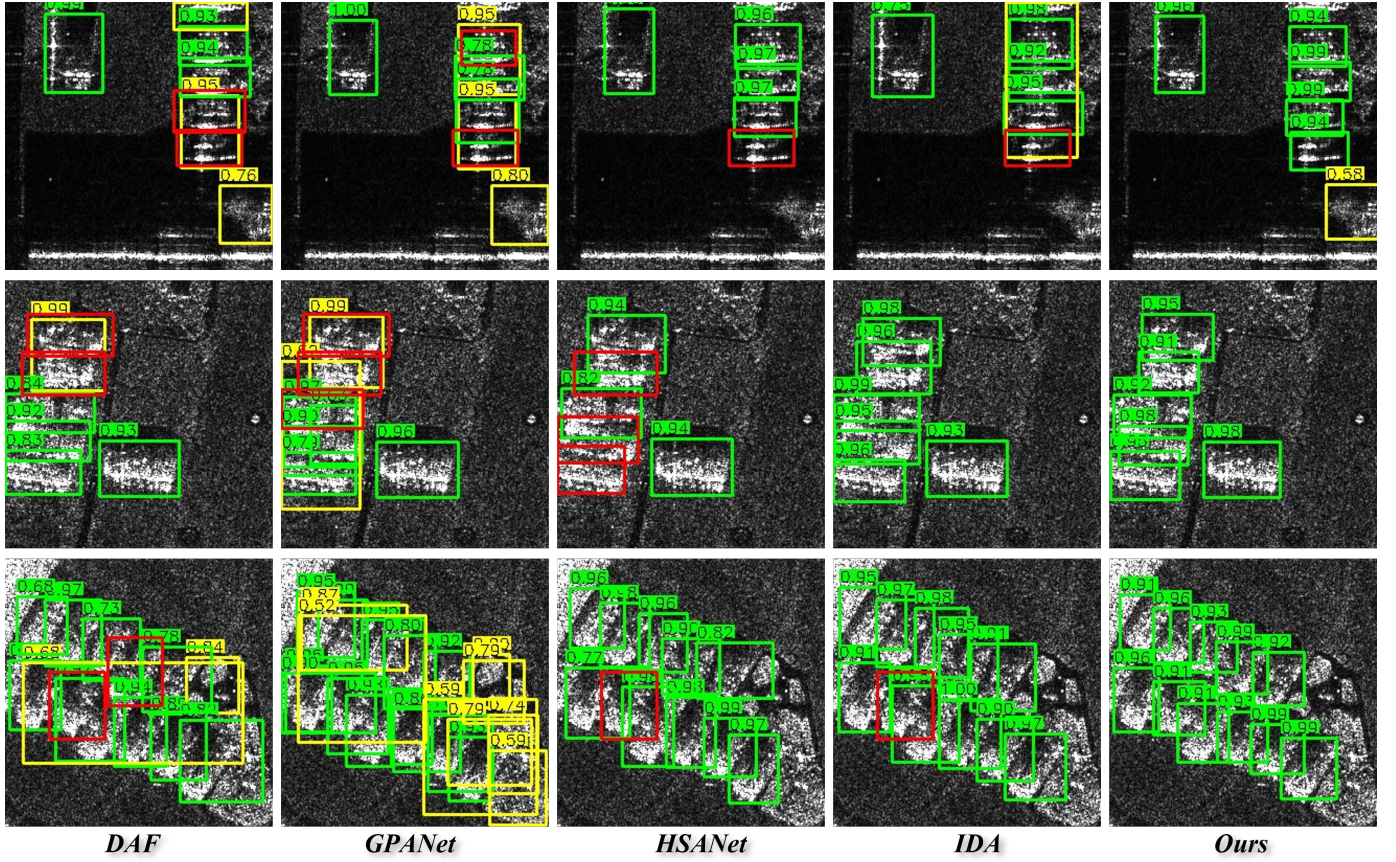


Fig. 15. Detection visualizations of different methods on the Vehicle LR→HR task. Here, in all subfigures, the green, yellow and red rectangular boxes denote correct detections, false alarms and miss detections respectively.

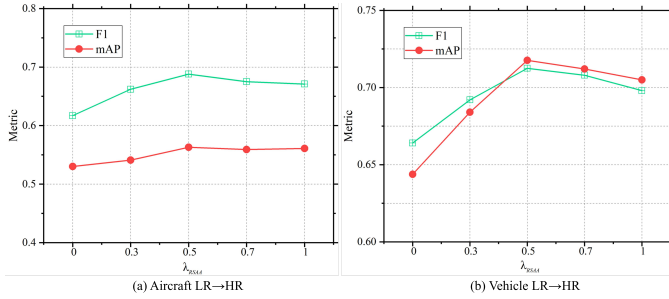


Fig. 16. Hyperparameter discussions of  $\lambda_{RSAA}$ .

When  $\lambda_{RSAA} > 0.5$ , the performance tends to level off or even decline, suggesting that further increasing  $\lambda_{RSAA}$  provides limited benefits, and the excessive alignment may even restrict the generalization ability. Therefore, setting  $\lambda_{RSAA}$  to around 0.5 can ensure satisfactory cross-resolution detection performance.

Fig. 17 illustrates the impact of the hyperparameter  $r$  on detection performance. In the Aircraft LR→HR task, as  $r$  increases from 0 to 5, both F1 and mAP rise to their highest values. However, when  $r$  continues to increase beyond this point, neither F1 nor mAP improves further, suggesting that excessive number of source domain neighbors offer limited benefits for the discriminative performance improvement. For the Vehicle LR→HR task, the optimal F1 and mAP are observed when  $r = 3$ , with a slight decrease in performance as

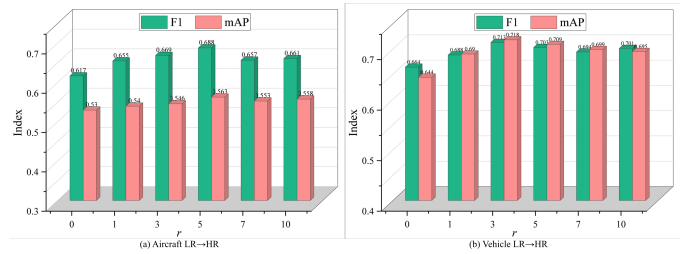


Fig. 17. Hyperparameter discussions of  $r$ .  $r = 0$  means RSAA module is not used during the training process.

$r$  increases further. These results demonstrate that, during the adjacency semantic alignment process, selecting a moderate number of source domain neighbors can effectively balance the strength of alignment and the influence of noise, thereby maximizing detection performance. In contrast, using too few or too many source neighbors does not provide additional performance improvements.

Fig. 19 illustrates the impact of the hyper-parameters  $k$  and  $\lambda_{se}$  on cross-resolution detection performance.  $k$  acts as a scaling factor for the reliable instance factor  $\hat{\eta}$  in Eq.14, directly influencing the strength of adjacency alignment. Meanwhile,  $\lambda_{se}$  determines the selection range of the secure adjacency set in Eq. 15. As shown in Fig. 19, the F1 score reaches its maximum when  $k = 30$  and  $\lambda_{se} = -1$ . When  $k = 0$ ,



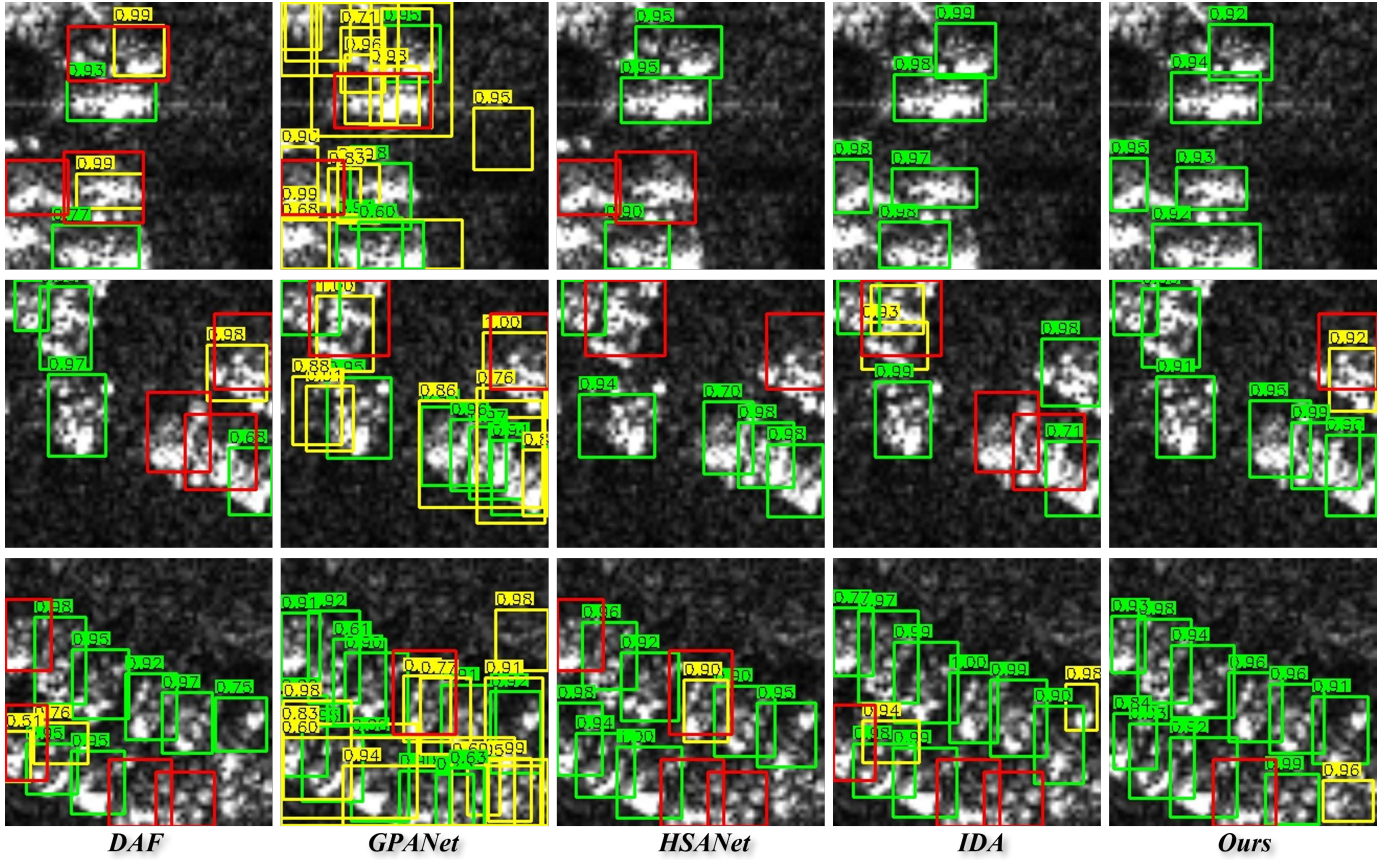


Fig. 18. Detection visualizations of different methods on the Vehicle HR→LR task. Here, in all subfigures, the green, yellow and red rectangular boxes denote correct detections, false alarms and miss detections respectively.

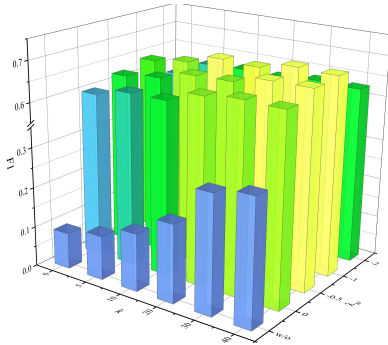


Fig. 19. Hyperparameter discussions of  $k$  and  $\lambda_{se}$ .

the model loses its ability to distinguish between reliable and unreliable instances. As a result, the adjacency alignment process treats all instances equally, leading to the accumulation of errors. An excessively large  $\lambda_{se}$  causes the secure set to include more risky information, which leads to error propagation and weakens the model's discriminative capability. Conversely, a small  $\lambda_{se}$  filters out too many informative instances, thereby degrading the adjacency alignment performance.

## VI. CONCLUSION

In this paper, we present a novel SAR target detection framework (*CR-Net*) that effectively addresses the challenges

of cross-resolution SAR detection. *CR-Net* achieves reliable cross-resolution detection by incorporating evidential learning theory and target scattering structure correlations, thereby evolving into two key modules: Structure-induced Hierarchical Feature Adaptation (*SHFA*) and Reliable Structural Adjacency Alignment (*RSAA*). Specifically, By exploring multi-mode structures within the domain, *CR-Net* integrates *SHFA* to perform fine-grained distribution adaptation under the guidance of structure similarity, thereby alleviating feature misalignment and enhancing the interpretability of the adaptation process. Furthermore, *RSAA* is integrated to improve the discriminability and generalization ability of *CR-Net* by transferring the discriminative information from source reliable adjacency samples. This dual approach enables *CR-Net* to significantly promote positive transfer while avoiding negative transfer. Extensive experimental results demonstrate that *CR-Net* substantially improves the performance of cross-resolution SAR target detection. In the future, we will continue to explore how to leverage foundation models to further enhance cross-resolution target detection performance, thereby promoting the practical application of this technology.

## REFERENCES

- [1] A. Moreira, P. Prats-Iraola, M. Younis, G. Krieger, I. Hajnsek, and K. P. Papathanassiou, "A tutorial on synthetic aperture radar," *IEEE Geoscience and Remote Sensing Magazine*, vol. 1, no. 1, pp. 6–43, 2013.

- [2] M. Long, Y. Cao, J. Wang, and M. Jordan, "Learning transferable features with deep adaptation networks," in *International conference on machine learning*. PMLR, 2015, pp. 97–105.
- [3] Y. Ganin and V. Lempitsky, "Unsupervised domain adaptation by back-propagation," in *International conference on machine learning*. PMLR, 2015, pp. 1180–1189.
- [4] B. Pan, Z. Xu, T. Shi, T. Li, and Z. Shi, "An imbalanced discriminant alignment approach for domain adaptive SAR ship detection," *IEEE Transactions on Geoscience and Remote Sensing*, vol. 61, pp. 1–11, 2023.
- [5] J. Zhang, S. Li, Y. Dong, B. Pan, and Z. Shi, "Hierarchical similarity alignment for domain adaptive ship detection in SAR images," *IEEE Transactions on Geoscience and Remote Sensing*, vol. 60, pp. 1–11, 2022.
- [6] H. Huang, J. Guo, H. Lin, Y. Huang, and X. Ding, "Domain Adaptive Oriented Object Detection from Optical to SAR Images," *IEEE Transactions on Geoscience and Remote Sensing*, 2024.
- [7] X. Zhang, S. Zhang, Z. Sun, C. Liu, Y. Sun, K. Ji, and G. Kuang, "Cross-Sensor SAR Image Target Detection Based on Dynamic Feature Discrimination and Center-Aware Calibration," *IEEE Transactions on Geoscience and Remote Sensing*, 2025.
- [8] Y. Shi, L. Du, and Y. Guo, "Unsupervised domain adaptation for SAR target detection," *IEEE Journal of Selected Topics in Applied Earth Observations and Remote Sensing*, vol. 14, pp. 6372–6385, 2021.
- [9] B. Zou, J. Qin, and L. Zhang, "Cross-scene target detection based on feature adaptation and uncertainty-aware pseudo-label learning for high resolution SAR images," *ISPRS Journal of Photogrammetry and Remote Sensing*, vol. 200, pp. 173–190, 2023.
- [10] S. Zhao, Z. Zhang, W. Guo, and Y. Luo, "An automatic ship detection method adapting to different satellites SAR images with feature alignment and compensation loss," *IEEE Transactions on Geoscience and Remote Sensing*, vol. 60, pp. 1–17, 2022.
- [11] S. Zhao, Y. Luo, T. Zhang, W. Guo, and Z. Zhang, "A feature decomposition-based method for automatic ship detection crossing different satellite SAR images," *IEEE Transactions on Geoscience and Remote Sensing*, vol. 60, pp. 1–15, 2022.
- [12] C. Chen, Z. Zheng, X. Ding, Y. Huang, and Q. Dou, "Harmonizing Transferability and Discriminability for Adapting Object Detectors," in *2020 IEEE/CVF Conference on Computer Vision and Pattern Recognition (CVPR)*, 2020, pp. 8866–8875.
- [13] S. Kim, J. Choi, T. Kim, and C. Kim, "Self-training and adversarial background regularization for unsupervised domain adaptive one-stage object detection," in *Proceedings of the IEEE/CVF international conference on computer vision*, 2019, pp. 6092–6101.
- [14] L. Zhang, Y. Liu, W. Zhao, X. Wang, G. Li, and Y. He, "Frequency-adaptive learning for SAR ship detection in clutter scenes," *IEEE Transactions on Geoscience and Remote Sensing*, vol. 61, pp. 1–14, 2023.
- [15] Z. Wang, L. Du, J. Mao, B. Liu, and D. Yang, "SAR target detection based on SSD with data augmentation and transfer learning," *IEEE Geoscience and Remote Sensing Letters*, vol. 16, no. 1, pp. 150–154, 2018.
- [16] B. Zou, J. Qin, and L. Zhang, "Vehicle Detection Based on Semantic-Context Enhancement for High-Resolution SAR Images in Complex Background," *IEEE Geoscience and Remote Sensing Letters*, vol. 19, pp. 1–5, 2022.
- [17] M. Sensoy, L. Kaplan, and M. Kandemir, "Evidential deep learning to quantify classification uncertainty," *Advances in neural information processing systems*, vol. 31, 2018.
- [18] Z. Gao, X. Jiang, X. Xu, F. Shen, Y. Li, and H. T. Shen, "Embracing unimodal aleatoric uncertainty for robust multimodal fusion," in *Proceedings of the IEEE/CVF Conference on Computer Vision and Pattern Recognition*, 2024, pp. 26 876–26 885.
- [19] J. Pei, A. Men, Y. Liu, X. Zhuang, and Q. Chen, "Evidential multi-source-free unsupervised domain adaptation," *IEEE Transactions on Pattern Analysis and Machine Intelligence*, vol. 46, no. 8, pp. 5288–5305, 2024.
- [20] W. J. Maddox, P. Izmailov, T. Garipov, D. P. Vetrov, and A. G. Wilson, "A simple baseline for bayesian uncertainty in deep learning," *Advances in neural information processing systems*, vol. 32, 2019.
- [21] Y. Gal and Z. Ghahramani, "Dropout as a bayesian approximation: Representing model uncertainty in deep learning," in *international conference on machine learning*. PMLR, 2016, pp. 1050–1059.
- [22] B. Lakshminarayanan, A. Pritzel, and C. Blundell, "Simple and scalable predictive uncertainty estimation using deep ensembles," *Advances in neural information processing systems*, vol. 30, 2017.
- [23] Q. Zhang, H. Wu, C. Zhang, Q. Hu, H. Fu, J. T. Zhou, and X. Peng, "Provable dynamic fusion for low-quality multimodal data," in *International conference on machine learning*. PMLR, 2023, pp. 41 753–41 769.
- [24] J. Chen, B. Ma, H. Cui, and Y. Xia, "Think Twice Before Selection: Federated Evidential Active Learning for Medical Image Analysis with Domain Shifts," in *2024 IEEE/CVF Conference on Computer Vision and Pattern Recognition (CVPR)*, 2024, pp. 11 439–11 449.
- [25] C. Huang, W. Huang, Q. Jiang, W. Wang, J. Wen, and B. Zhang, "Multimodal Evidential Learning for Open-World Weakly-Supervised Video Anomaly Detection," *IEEE Transactions on Multimedia*, pp. 1–12, 2025.
- [26] T.-Y. Lin, P. Goyal, R. Girshick, K. He, and P. Dollár, "Focal loss for dense object detection," in *Proceedings of the IEEE international conference on computer vision*, 2017, pp. 2980–2988.
- [27] J. Redmon and A. Farhadi, "Yolov3: An incremental improvement," *arXiv preprint arXiv:1804.02767*, 2018.
- [28] C.-Y. Wang, A. Bochkovskiy, and H.-Y. M. Liao, "Yolov7: Trainable bag-of-freebies sets new state-of-the-art for real-time object detectors," in *Proceedings of the IEEE/CVF conference on computer vision and pattern recognition*, 2023, pp. 7464–7475.
- [29] W. Liu, D. Anguelov, D. Erhan, C. Szegedy, S. Reed, C.-Y. Fu, and A. C. Berg, "Ssd: Single shot multibox detector," in *Computer Vision—ECCV 2016: 14th European Conference, Amsterdam, The Netherlands, October 11–14, 2016, Proceedings, Part I 14*. Springer, 2016, pp. 21–37.
- [30] S. Ren, K. He, R. Girshick, and J. Sun, "Faster r-cnn: Towards real-time object detection with region proposal networks," *Advances in neural information processing systems*, vol. 28, 2015.
- [31] P. Sun, R. Zhang, Y. Jiang, T. Kong, C. Xu, W. Zhan, M. Tomizuka, L. Li, Z. Yuan, C. Wang *et al.*, "Sparse r-cnn: End-to-end object detection with learnable proposals," in *Proceedings of the IEEE/CVF conference on computer vision and pattern recognition*, 2021, pp. 14 454–14 463.
- [32] Y. Zhou, H. Liu, F. Ma, Z. Pan, and F. Zhang, "A Sidelobe-Aware Small Ship Detection Network for Synthetic Aperture Radar Imagery," *IEEE Transactions on Geoscience and Remote Sensing*, vol. 61, pp. 1–16, 2023.
- [33] M. Ju, B. Niu, and J. Zhang, "FPDDet: An Efficient Rotated SAR Ship Detector Based on Simple Polar Encoding and Decoding," *IEEE Transactions on Geoscience and Remote Sensing*, vol. 61, pp. 1–15, 2023.
- [34] D. Zhao, Z. Chen, Y. Gao, and Z. Shi, "Classification Matters More: Global Instance Contrast for Fine-Grained SAR Aircraft Detection," *IEEE Transactions on Geoscience and Remote Sensing*, vol. 61, pp. 1–15, 2023.
- [35] J. Qin, B. Zou, Y. Chen, H. Li, and L. Zhang, "Scattering Attribute Embedded Network for Few-Shot SAR ATR," *IEEE Transactions on Aerospace and Electronic Systems*, 2024.
- [36] Y. Yang, Y. Du, L. Zhang, G. Li, Y. Chen, G. Cheng, and S. Song, "DAFDet: A Unified Dynamic SAR Target Detection Architecture With Asymptotic Fusion Enhancement and Feature Encoding Decoupling," *IEEE Transactions on Geoscience and Remote Sensing*, vol. 63, pp. 1–22, 2025.
- [37] Z. Cui, Q. Li, Z. Cao, and N. Liu, "Dense Attention Pyramid Networks for Multi-Scale Ship Detection in SAR Images," *IEEE Transactions on Geoscience and Remote Sensing*, vol. 57, no. 11, pp. 8983–8997, 2019.
- [38] J. Cheng, D. Xiang, J. Tang, Y. Zheng, D. Guan, and B. Du, "Inshore ship detection in large-scale SAR images based on saliency enhancement and Bhattacharyya-like distance," *Remote Sensing*, vol. 14, no. 12, p. 2832, 2022.
- [39] L. Zhang, Y. Liu, W. Zhao, X. Wang, G. Li, and Y. He, "Frequency-Adaptive Learning for SAR Ship Detection in Clutter Scenes," *IEEE Transactions on Geoscience and Remote Sensing*, vol. 61, pp. 1–14, 2023.
- [40] Y. Dai, M. Zou, Y. Li, X. Li, K. Ni, and J. Yang, "DenoDet: Attention as Deformable Multisubspace Feature Denoising for Target Detection in SAR Images," *IEEE Transactions on Aerospace and Electronic Systems*, vol. 61, no. 2, pp. 4729–4743, 2025.
- [41] Y. Suo, Y. Wu, T. Miao, W. Diao, X. Sun, and K. Fu, "Adaptive SAR Image Enhancement for Aircraft Detection via Speckle Suppression and Channel Combination," *IEEE Transactions on Geoscience and Remote Sensing*, vol. 62, pp. 1–15, 2024.
- [42] Z. Pei, Z. Cao, M. Long, and J. Wang, "Multi-adversarial domain adaptation," in *Proceedings of the AAAI conference on artificial intelligence*, vol. 32, no. 1, 2018.

- [43] M. Khodabandeh, A. Vahdat, M. Ranjbar, and W. G. Macready, "A robust learning approach to domain adaptive object detection," in *Proceedings of the IEEE/CVF international conference on computer vision*, 2019, pp. 480–490.
- [44] K. Bousmalis, N. Silberman, D. Dohan, D. Erhan, and D. Krishnan, "Unsupervised pixel-level domain adaptation with generative adversarial networks," in *Proceedings of the IEEE conference on computer vision and pattern recognition*, 2017, pp. 3722–3731.
- [45] J. Qin, K. Wang, B. Zou, L. Zhang, and J. van de Weijer, "Conditional Diffusion Model with Spatial-Frequency Refinement for SAR-to-Optical Image Translation," *IEEE Transactions on Geoscience and Remote Sensing*, 2024.
- [46] J. Deng, W. Li, Y. Chen, and L. Duan, "Unbiased mean teacher for cross-domain object detection," in *Proceedings of the IEEE/CVF conference on computer vision and pattern recognition*, 2021, pp. 4091–4101.
- [47] M. Kennerley, J.-G. Wang, B. Veeravalli, and R. T. Tan, "Cat: Exploiting inter-class dynamics for domain adaptive object detection," in *Proceedings of the IEEE/CVF Conference on Computer Vision and Pattern Recognition*, 2024, pp. 16 541–16 550.
- [48] J. Deng, D. Xu, W. Li, and L. Duan, "Harmonious teacher for cross-domain object detection," in *Proceedings of the IEEE/CVF conference on computer vision and pattern recognition*, 2023, pp. 23 829–23 838.
- [49] J. Qin, S. Li, A. Gomez-Villa, S. Yang, Y. Wang, K. Wang, and J. van de Weijer, "Free-lunch color-texture disentanglement for stylized image generation," *arXiv preprint arXiv:2503.14275*, 2025.
- [50] T. Zhang, D. Wang, H. Chen, Z. Zeng, W. Guo, C. Miao, and L. Cui, "BDANN: BERT-Based Domain Adaptation Neural Network for Multi-Modal Fake News Detection," in *2020 International Joint Conference on Neural Networks (IJCNN)*, 2020, pp. 1–8.
- [51] L. Zhang, X. Wang, D. Yang, T. Sanford, S. Harmon, B. Turkbey, B. J. Wood, H. Roth, A. Myronenko, D. Xu, and Z. Xu, "Generalizing Deep Learning for Medical Image Segmentation to Unseen Domains via Deep Stacked Transformation," *IEEE Transactions on Medical Imaging*, vol. 39, no. 7, pp. 2531–2540, 2020.
- [52] C. Chen, Q. Dou, H. Chen, J. Qin, and P. A. Heng, "Unsupervised Bidirectional Cross-Modality Adaptation via Deeply Synergistic Image and Feature Alignment for Medical Image Segmentation," *IEEE Transactions on Medical Imaging*, vol. 39, no. 7, pp. 2494–2505, 2020.
- [53] Z. Yue, Q. Sun, X.-S. Hua, and H. Zhang, "Transporting causal mechanisms for unsupervised domain adaptation," in *Proceedings of the IEEE/CVF International Conference on Computer Vision*, 2021, pp. 8599–8608.
- [54] J. Qin, B. Zou, H. Li, and L. Zhang, "Efficient End-to-End Diffusion Model for One-Step SAR-to-Optical Translation," *IEEE Geoscience and Remote Sensing Letters*, vol. 22, pp. 1–5, 2025.
- [55] Y. Shi, L. Du, Y. Guo, and Y. Du, "Unsupervised domain adaptation based on progressive transfer for ship detection: From optical to SAR images," *IEEE Transactions on Geoscience and Remote Sensing*, vol. 60, pp. 1–17, 2022.
- [56] S. Liu, D. Li, J. Wan, C. Zheng, J. Su, H. Liu, and H. Zhu, "Source-Assisted Hierarchical Semantic Calibration Method for Ship Detection Across Different Satellite SAR Images," *IEEE Transactions on Geoscience and Remote Sensing*, vol. 62, pp. 1–21, 2024.
- [57] J.-Y. Zhu, T. Park, P. Isola, and A. A. Efros, "Unpaired image-to-image translation using cycle-consistent adversarial networks," in *Proceedings of the IEEE international conference on computer vision*, 2017, pp. 2223–2232.
- [58] J. Dong, J. Feng, and X. Tang, "OptiSAR-Net: A Cross-Domain Ship Detection Method for Multisource Remote Sensing Data," *IEEE Transactions on Geoscience and Remote Sensing*, vol. 62, pp. 1–11, 2024.
- [59] Y. Rubner, C. Tomasi, and L. J. Guibas, "The earth mover's distance as a metric for image retrieval," *International journal of computer vision*, vol. 40, pp. 99–121, 2000.
- [60] M. Cuturi, "Sinkhorn distances: Lightspeed computation of optimal transport," *Advances in neural information processing systems*, vol. 26, 2013.
- [61] L. Van der Maaten and G. Hinton, "Visualizing data using t-sne," *Journal of machine learning research*, vol. 9, no. 11, 2008.
- [62] Y. Chen, W. Li, C. Sakaridis, D. Dai, and L. Van Gool, "Domain adaptive faster r-cnn for object detection in the wild," in *Proceedings of the IEEE conference on computer vision and pattern recognition*, 2018, pp. 3339–3348.
- [63] W. Zhirui, K. Yuzhuo, Z. Xuan, W. Yuelei, Z. Ting, and S. Xian, "Sar-aircraft-1.0: High-resolution sar aircraft detection and recognition dataset," *Journal of Radars*, vol. 12, no. 4, pp. 906–922, 2023.
- [64] P. Zhang, H. Xu, T. Tian, P. Gao, L. Li, T. Zhao, N. Zhang, and J. Tian, "Sefepnet: Scale expansion and feature enhancement pyramid network for sar aircraft detection with small sample dataset," *IEEE Journal of Selected Topics in Applied Earth Observations and Remote Sensing*, vol. 15, pp. 3365–3375, 2022.
- [65] FARADSAR public Release Data. [Online]. Available: [https://www.sandia.gov/radar/complex\\_data/FARAD\\_KA\\_BAND.zip](https://www.sandia.gov/radar/complex_data/FARAD_KA_BAND.zip).
- [66] M. Xu, H. Wang, B. Ni, Q. Tian, and W. Zhang, "Cross-domain detection via graph-induced prototype alignment," in *Proceedings of the IEEE/CVF Conference on Computer Vision and Pattern Recognition*, 2020, pp. 12 355–12 364.